Radiative proton capture to low-lying $T = 0$ and $T = 1$ states in ^{10}B

D. R. Chakrabarty,[1,*] V. M. Datar,[2] Suresh Kumar,[1] E. T. Mirgule,[3] G. Mishra,[3,4] P. C. Rout,[3,4] C. Ghosh,[5] V. Nanal,[5] S. Joshi,[3,4] and R. Kujur[3]

[1]*(Ex)Nuclear Physics Division, Bhabha Atomic Research Centre, Mumbai 400 085, India*
[2]*INO Cell, Tata Institute of Fundamental Research, Mumbai 400 005, India*
[3]*Nuclear Physics Division, Bhabha Atomic Research Centre, Mumbai 400 085, India*
[4]*Homi Bhabha National Institute, Anushaktinagar, Mumbai 400 094, India*
[5]*Department of Nuclear and Atomic Physics, Tata Institute of Fundamental Research, Mumbai 400 005, India*

(Received 19 November 2016; published 31 January 2017)

Cross sections of the radiative proton capture reaction ^{9}Be(p,γ), leading to the low-lying excited states in ^{10}B with isospin $T = 0$ and 1, have been measured over the proton energy range of 7 to 20 MeV. For this, the method of coincidence between the primary and the secondary γ rays has been used. These γ rays are emitted following, respectively, the proton capture to an excited state and the subsequent decay of that state. A direct-semidirect capture model calculation has been performed and compared with the experimental data. The experimental results do not show a strong isospin dependence of the GDR strength function built on the low-lying states. The derived photoproton cross sections on these states and the earlier-measured photoneutron cross sections on the ground state of ^{10}B show a large difference.

DOI: 10.1103/PhysRevC.95.014614

I. INTRODUCTION

The radiative proton capture reaction has been studied for many years, yielding valuable information on the giant electric dipole resonance (GDR), built on the ground and excited states in nuclei, and the single-particle structure of the nuclear states [1,2]. The GDRs built on discrete and continuum states have also been extensively studied [1,3–5] using various other probes. The study of the GDR built on the isobaric analog states, which is another interesting mode of excitation in nuclei, has been made using the pion double charge exchange reactions [6]. The radiative proton capture reaction is also a tool to study this process. To our knowledge, however, only two such studies have been published so far. These are on the GDR built on the isospin $T = 1$ states in self-conjugate nuclei ^{14}N (at 2.31 MeV) [7,8] and ^{12}C (at 15.11 MeV) [9,10].

The GDR built on a state of isospin T in a nucleus with $|T_3| \leqslant T - 1$ can have isospin $T_{\rm GDR} = T - 1$, T, or $T + 1$. Here, $T_3 = (N - Z)/2$ is the third component of isospin and N and Z are the neutron and proton numbers, respectively, of the nucleus. These three isospin components are expected to be at different excitation energies due to the isospin splitting of the GDR [11,12]. In a self-conjugate nucleus ($T_3 = 0$), the GDR built on the $T = 1$ state can only have $T_{\rm GDR} = 0$ or 2. This happens because, in this case, the isospin selection rule for the isovector electric dipole ($E1$) transition forbids the transition with $\Delta T = 0$. In the radiative proton capture reaction, forming a self-conjugate nucleus, the excitation of the $T_{\rm GDR} = 2$ component is also isospin forbidden because both the target and the projectile have $T = 1/2$. Assuming a small isospin mixing in the entrance channel, the excited GDR has predominantly $T_{\rm GDR} = 0$. On the other hand, the GDR built on the $T = 0$ states can have $T_{\rm GDR} = 1$ only. Thus, if the isospin splitting is very prominent, the GDRs built on the $T = 0$ and 1 states are expected to have different energies. However, particularly in light nuclei, the GDR strength is often not concentrated in a narrow energy region and the above expectation can be influenced by detailed structure effects. Another aspect to consider is that the first $T = 1$ state in a self-conjugate nucleus is the isobaric analog of the ground state of the neighboring unstable nuclei with $|T_3| = 1$. In the photoabsorption experiments on these nuclei, only the $T_{\rm GDR} = 1$ and 2 components can be excited. From a comparison of the results from all these experiments, it may be possible to address the isospin splitting into all three components.

We have made measurements of the radiative proton capture reaction ^{9}Be(p,γ), over the proton energy (E_p) range of 7 to 20 MeV, in order to address the above issues for the self-conjugate nucleus ^{10}B. This reaction was studied [13,14] earlier at low proton energies ($E_p < 4$ MeV). In the range of $E_p = 4$–18 MeV, the measurement was reported only in an unpublished thesis [14].

In a singles measurement of the high-energy γ rays produced in the radiative capture reactions, it is difficult to discriminate clearly between the primary γ-ray transitions to different final states if the latter are not well separated in energy. This is because of the broad line shape of the γ-ray detector (of a practical size) arising from the leakage of the electron and γ-ray shower produced after the primary interaction of the incident photon. If the final states are particle-bound, these subsequently decay by emitting secondary low-energy γ rays. A measurement made in coincidence with these secondary low-energy γ rays, being detected in a detector with good energy resolution, can, in principle, separate the primary transitions to the closely-spaced final states.

In ^{10}B, the five low-lying excited states, which are particle bound or decay predominantly by emitting γ rays, are shown in Fig. 1. The first $T = 1$ state is at 1.74 MeV in close vicinity of the state at 2.154 MeV. As mentioned above, it is difficult

*dr_chakrabarty@yahoo.com

 ©2017 American Physical Society

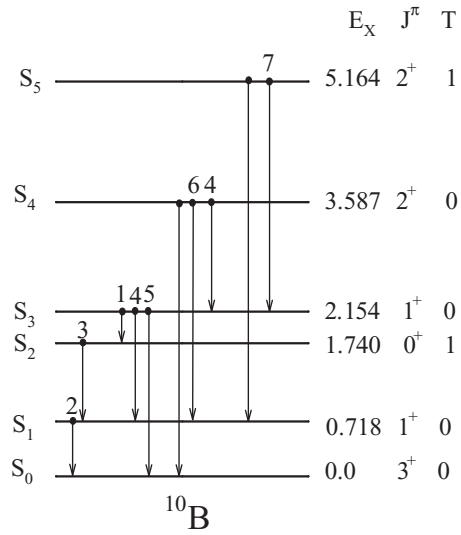

FIG. 1. Low-lying levels in ^{10}B (designated as S_0 to S_5) relevant for the present work with their excitation energy (E_X) in MeV, spin-parity (J^π) and isospin (T). Arrows indicate the main γ decay branches. The numbers refer to the γ rays used in the present analysis (see also Table III).

to discriminate clearly between the primary γ-ray transitions to these states with a practical high-energy γ-ray detector. We have, therefore, made the measurements in coincidence with the secondary low-energy γ rays. The second $T = 1$ state is at 5.164 MeV. Although this state is above the α-particle separation energy, it decays predominantly via γ-ray emission with a branching ratio >80%. This happens because the α-particle emission is suppressed due to the violation of the isospin conservation rule.

The present work describes the measurement of the cross sections of the ^{9}Be(p,γ) reaction populating the above-mentioned $T = 0$ and $T = 1$ states in ^{10}B. The main motivation is to study the GDR built on these states and to address the difference, if any, between the GDR strength functions with $T_{\rm GDR} = 1$ and 0, respectively.

II. EXPERIMENTAL DETAILS

The experiment was performed at the Pelletron Linac Facility (PLF), Mumbai, with the proton beam from the Pelletron accelerator bombarding self-supporting beryllium foils of thickness 1.1–4.5 mg/cm^2. The primary high-energy γ rays were detected in a close-packed array of 19 hexagonal bismuth germanate (BGO) detectors, each with a face-to-face distance of ~5.8 cm and length 7.6 cm. Secondary low-energy γ rays were detected in two cylindrical $LaBr_3$(Ce) detectors (henceforth referred to as LaBr detectors) of diameter 7.6 cm and length 15.2 cm. The BGO array was kept at 90° to the beam direction and at a distance of 7.3 cm from the target. The LaBr detectors were kept at 135°, on either side of the beam, and at a distance of 6.2 cm from the target. These were placed on a plane perpendicular to the BGO-array axis. Part of the data was taken with one LaBr detector kept at 90°, opposite to the BGO array, and at a distance of 7.3 cm. Adequate lead and borated paraffin shielding was arranged to reduce the beam-induced neutron and γ-ray backgrounds from the upstream collimators and the beam dump. Besides the main measurements on the Be target, the characterization of the detectors was done by the measurements with Al (self-supporting) and natural B (on thick Ta) targets. Table I lists the targets used at different proton energies, the latter being estimated at the center of the target. The energy loss of the proton beam in the targets ranged from ~50 to 170 keV.

TABLE I. Proton energies and targets used in the experiment. $\langle E_p \rangle$ is the proton energy at the center of the target. E_X^C is the mean excitation energy in the compound system.

Target	Thickness (mg/cm^2)	$\langle E_p \rangle$ (MeV)	E_X^C (MeV)
Be	1.1	7.98	13.76
Be	2.0	7.0–8.8	12.89–14.51
		8.96	14.65
		11.0	16.49
		13.0	18.29
		13.97	19.16
		15.0	20.09
		15.97	20.96
		17.98	22.77
Be	4.3	17.0	21.89
Be	4.5	9.91	15.50
		11.91	17.30
		19.95	24.54
Al	1.9	7.96	19.26
		8.97	20.23
		9.96	22.19
B	~0.6	7.98	23.28

The measurements were made in the coincidence mode with the Be target and mainly in the singles mode with the other targets. In the case of the Al target, the measurement at $E_p = 7.96$ MeV was also made in the coincidence mode. In this mode, the event trigger was generated from a fast coincidence between the OR signal from the BGO array (generated when at least one detector fires) and that from either of the LaBr detectors (matched in time). Time-to-digital converters (TDC) were used to record the timing (T_{BG}) between either of the LaBr detectors (start) and the individual BGO detectors (stop). The time resolution for each detector was ~3 ns. The energy deposited in each detector was recorded with a charge to digital converter (QDC). The pulse pileup in each BGO detector was measured by using the integrated energy signals in two QDCs with a short (200 ns) and a long (2 μs) gate. The latter was taken as the measure of the total deposited energy in the detector. The two-dimensional (2D) spectrum of the QDC outputs with the short gate (Q_S) and the long gate (Q_L) is diagonal for events with no pileup. A 2D gate corresponding to the non-pileup events was applied to select the acceptable events in the data analysis. In the singles mode of the data acquisition, only the BGO signals were recorded. The energy calibration with radioactive sources was carried out in the singles mode using both BGO and LaBr signals.

A VME-based data acquisition system was used to record the data in an event-by-event mode. The parameters recorded

for each event were the 40 QDC outputs (two for each BGO and one for each LaBr) and the 19 TDC outputs. In the singles mode, the 19 TDC outputs were generated using the OR signal from the BGO array as the start signal. A calibrated pulser of frequency 10 Hz was used to assess the dead time in the data acquisition process. Data was collected in the proton energy steps ranging from 0.2 to 2 MeV. The smaller energy step was taken for $E_p = 7$–9 MeV because a preliminary measurement suggested an excess yield around $E_p = 8$ MeV. The total incident charge on the target at various proton energies varied from ∼40 to 250 μC.

The relevant γ-ray energies for the BGO detectors were in the range of ∼8 to 24 MeV. The energy calibration of the detectors was done with radioactive sources ^{22}Na and ^{241}Am-Be emitting γ rays of energy 0.511 to 4.44 MeV and (p,γ) reaction on B and Al targets producing γ rays of energy up to ∼23.3 MeV. The voltage applied to the photomultiplier tubes (PMTs) of the BGO detectors was chosen so as to make the calibration reasonably linear up to ∼24 MeV. A small nonlinearity, assessed from the calibration measurements, was taken into account in the data analysis. For the LaBr detectors, the relevant energy range is up to 5 MeV. The radioactive sources used for the energy calibration were, besides those mentioned above, ^{137}Cs, ^{60}Co, and ^{238}Pu -^{13}C emitting γ rays of energy up to 6.13 MeV. A lower voltage was applied to the PMTs and the calibration was linear at least up to 6.13 MeV. The gain variation of the detectors was periodically monitored with the radioactive sources and was taken into account in the data analysis.

III. EXPERIMENTAL DATA ANALYSIS

In the analysis of the experimental data, first, two sets of 2D spectra (Q_S vs Q_L and T_{BG} vs Q_L) were generated for each BGO detector. Two sets of 2D gates were defined on these spectra corresponding to the non-pileup and prompt-coincidence events, respectively. For each accepted event satisfying these two sets of gate conditions, the BGO detector with the highest energy deposition was identified and the energies deposited in the neighboring detectors were added to this energy to get the summed energy ($E_{\rm BGO}$). Finally, for the coincidence measurements, the 2D spectrum between $E_{\rm BGO}$ and the energy deposited in either of the LaBr detectors ($E_{\rm LaBr}$) was generated at each proton energy.

Before discussing the methods used to extract the capture cross-sections using the Be target, we address the comparison of the measured and simulated response functions of the BGO array for high-energy γ rays. The summed-energy spectra for the BGO array were generated, as explained above, from the singles measurements with Al and B targets. Some examples of these spectra are shown in Fig. 2 along with the simulated response functions calculated by using the electron-gamma-shower (EGS) computer code [15]. The EGS results were cross-checked with the GEANT simulations [16]. For the Al target, the simulations were done for the γ-ray energies corresponding to the transition to the ground state (γ_0), the first excited state at 1.78 MeV (γ_1), and the second excited state at 4.62 MeV (γ_2) in ^{28}Si. For the B target, the calculations were performed for the transitions to the ground state (γ_0) and the first excited

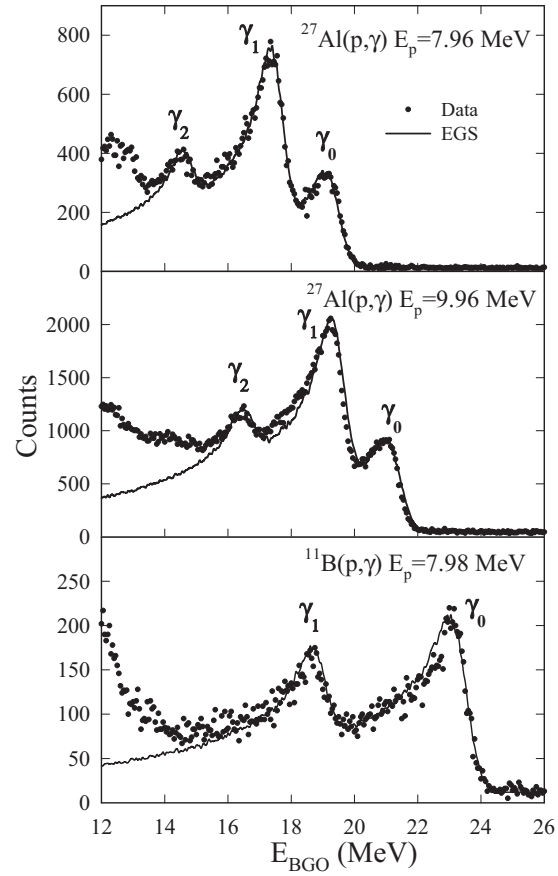

FIG. 2. Examples of the measured spectra and EGS simulations for different reactions. Peak positions of the γ rays originating from the transitions to the ground (γ_0) and the excited states (γ_1 and γ_2) are indicated. The right-hand-side pedestals in the data were added to the simulations.

state (γ_1) at 4.44 MeV in ^{12}C. The angular distribution of the γ rays [17,18] and the Doppler shifts were considered while performing the simulation calculations. Moreover, for the γ_1 and the γ_2 transitions, the summing effects due to the possible simultaneous detection of the secondary low-energy γ rays were considered. The cross sections for the various transitions were adjusted to get the absolute fits as exemplified by the solid lines in Fig. 2. The cross sections extracted from the best fits are tabulated in Table II. These agree reasonably well with the earlier measurements [17,18], providing confidence in using the EGS simulations for all relevant γ-ray energies.

TABLE II. Experimental cross sections derived from the data and EGS simulations. $\sigma_0, \sigma_1, \sigma_2$ correspond to the transitions to the ground, first, and second excited states, respectively.

Reaction	E_p (MeV)	σ_0 (μb)	σ_1 (μb)	σ_2 (μb)
$p + ^{27}$Al	7.96	24.2 ± 1.4	42.4 ± 1.7	12.4 ± 1.0
$p + ^{27}$Al	8.97	49.3 ± 1.6	87.6 ± 1.9	16.6 ± 1.6
$p + ^{27}$Al	9.96	57.2 ± 2.6	100.3 ± 3.5	30.0 ± 3.0
$p + ^{11}$B	7.99	105.4 ± 4.7	51.4 ± 2.6	

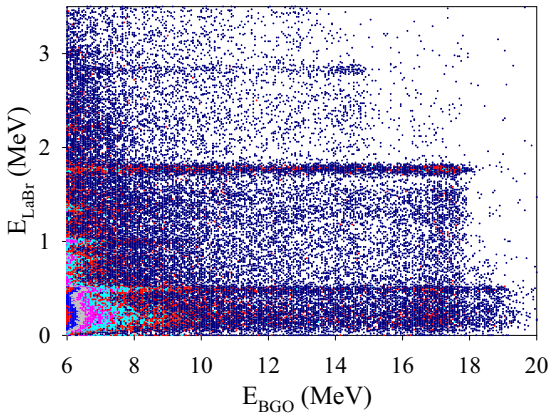

FIG. 3. Two-dimensional spectrum between the summed energy deposited in the BGO array and that deposited in either of the LaBr detectors at $E_p = 7.96$ MeV with the Al target.

The full-energy peak efficiencies for the detection of the secondary γ rays in the LaBr detectors were obtained from the calculated energy dependence of the efficiency using the EGS simulations and matching with the experimental efficiencies at 1.173 and 1.332 MeV. The latter quantities were derived from the singles and coincidence measurements using the radioactive ^{60}Co source and taking into account the angular correlation between the emitted γ rays. The efficiencies measured using two sources of different decay strengths (by a factor of $\sim$10) were consistent within 3%.

In order to benchmark the procedure of extracting the capture cross sections from the present measurements, the coincidence data taken with the Al target at $E_p = 7.96$ MeV were next analysed. Figure 3 shows the 2D spectrum of $E_{\rm LaBr}$ vs $E_{\rm BGO}$ for this target. The horizontal streaks signifying the detection of the 1.78 and 2.84 MeV γ rays in the LaBr detectors are clearly visible. These γ rays are emitted following the transitions from the first excited to the ground state and from the second excited to the first excited state, respectively, in ^{28}Si. The projected $E_{\rm BGO}$ spectrum, shown in Fig. 4, was generated by putting a gate on the 1.78 MeV peak on the $E_{\rm LaBr}$ axis and subtracting the pedestal contribution from the nearby regions. The EGS simulation, done assuming an isotropic emission of all the γ-rays, is also shown in the figure. This includes both γ_1 and γ_2 transitions. The latter was included because the 1.78 MeV γ ray also arises from the subsequent decay of the 4.62 MeV state, populated after the γ_2 transition. The absolute comparison of the data and the simulation, shown in Fig. 4, corresponds to $\sigma_1 = 42.6 \pm 3.6$ μb.

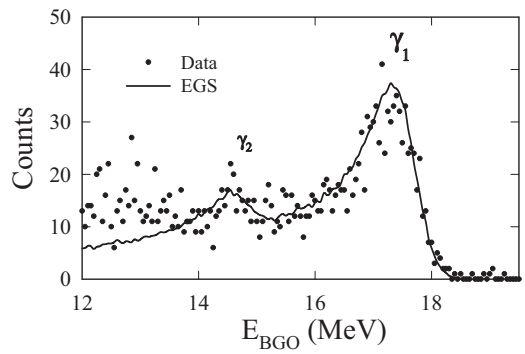

FIG. 4. BGO spectrum in coincidence with the 1.78 MeV γ ray detected in the LaBr from the Al target at $E_p = 7.96$ MeV. The EGS simulation is also shown. Peak positions of the γ rays originating from the transitions to the excited states (γ_1 and γ_2) are indicated.

The correction to the extracted cross-section due to the angular correlation between the primary and the secondary γ rays was calculated using Eqs. (2), (5), and (6) of Ref. [19]. The m-state population of the intial state J_1 was calculated as

$$P(J_1,m) = \sum_{S,m_t,l} (2l+1)T(l)\left\langle j_t m_t \frac{1}{2} m - m_t \middle| Sm \right\rangle^2 \langle Sml0|J_1 m\rangle^2, \quad (1)$$

where j_t and m_t are the target spin and its projection quantum number, S is the incoming channel spin, l is the orbital angular momentum of the proton and $T(l)$ is the transmission coefficient. The last quantity was calculated using the optical model potential (OMP) parameters of Ref. [20]. Assuming the emission of $E1$-radiation populating the final 2^+ state in this case, the initial state can have $J_1 = 1$–3 and a negative parity. Since both the target and the projectile have positive parities, the sum in Eq. (1) runs over only the odd values of l consistent with J_1 and S. As discussed in Ref. [18], the measured angular distribution of the primary γ rays, consistent with $a_1 \sim 0$ and $a_2 = -0.5$ [see Eq. (3) later for the definition of a_n coefficients], suggests mainly $J_1 = 2$. Using $J_1 = 2$ and the $P(m)$ values calculated from Eq. (1), the corrected cross section was estimated as $\sigma_1 = 42.0 \pm 3.5$ μb. By adjusting the $P(m)$ values in order to get the experimental a_2 for the primary γ rays (calculated by integrating Eq. (2) of Ref. [19] over the angles of the secondary γ rays), the corrected cross section was estimated as $\sigma_1 = 39.9 \pm 3.5$ μb. Thus, the extracted cross section from the coincidence measurement reasonably agrees with that from the singles measurement.

We now discuss the extraction of the capture cross-sections from the coincidence measurements with the Be target. Figure 5 shows an example of the 2D spectrum of $E_{\rm LaBr}$ vs $E_{\rm BGO}$ for this target. Here, also, the horizontal streaks

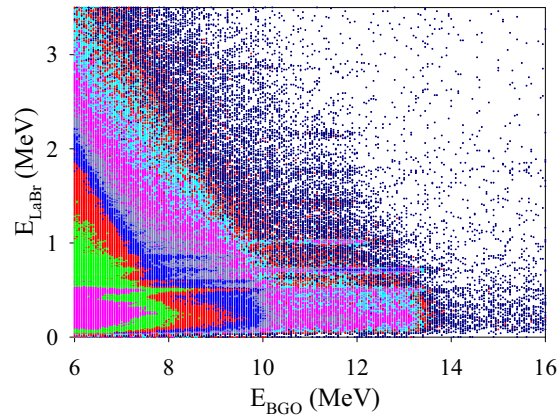

FIG. 5. Same as in Fig. 3 but for the 1.1 mg/cm^2 Be target at $E_p = 7.98$ MeV.

TABLE III. Low-energy γ rays detected in the LaBr and their possible origins from the different excited states in ^{10}B.

LaBr γ-ray no.	E_γ (MeV)	Transitions in ^{10}B	Possible parent states
1	0.414	$S_3 \rightarrow S_2$	S_3, S_4, S_5
2	0.718	$S_1 \rightarrow S_0$	S_1, S_2,S_3, S_4, S_5
3	1.022	$S_2 \rightarrow S_1$	S_2, S_3, S_4, S_5
4	1.435[a]	$S_3 \rightarrow S_1$	S_3, S_4, S_5
		$S_4 \rightarrow S_3$	
5	2.154	$S_3 \rightarrow S_0$	S_3, S_4, S_5
6	2.869	$S_4 \rightarrow S_1$	S_4, S_5
7	3.010	$S_5 \rightarrow S_3$	S_4, S_5
		$S_4 \rightarrow S_0$[b]	

[a]Unresolved 1.433 and 1.436 MeV.
[b]Unresolved first escape peak of 3.587 MeV.

correspond to the various low-energy γ rays, arising from the interstate transitions (Table III and Fig. 1) in ^{10}B, detected in the LaBr detectors. It is apparent that a high neutron production in the Be target leads to many background events in the 2D spectrum. However, the above procedure, of creating the $E_{\rm BGO}$ spectrum in coincidence with the low-energy γ-ray peaks and subtracting the spectrum in coincidence with the pedestal regions, removes the neutron-induced contribution, albeit in a statistical manner.

Table III lists the main low-energy γ rays, used in the present data analysis, arising from the transitions between the various low-lying excites states of ^{10}B as shown in Fig. 1. The designations of the states as S_0 to S_5 are explained in the same figure. The table also lists the possible parent states in ^{10}B for the origin of each γ ray. This, in turn, suggests the possible coincidences with the different primary γ ray transitions.

It is evident from Table III that each of the LaBr γ rays originates from a number of states and the corresponding coincident $E_{\rm BGO}$ spectra are, therefore, related to various σ_i values. Here, σ_i denotes the radiative capture cross section for the transition to the state S_i. This is illustrated in Fig. 6, which shows the $E_{\rm BGO}$ spectra in coincidence with different LaBr γ rays. The figure also shows the EGS simulations done for γ_1 to γ_3 with their contributions normalized to get the absolute fits to the data. Using these fits, the coincident yields corresponding to the transitions to various states can, in principle, be extracted. However, in practice, this leads to some uncertainty due to those in the normalization factors. This is particularly so for the case in which the coincident yield is low.

For the extraction of the capture cross-sections to different final states, the following procedure was adopted at each proton energy. Instead of projecting the 2D spectrum on the $E_{\rm BGO}$ axis, the spectrum was projected on the $E_{\rm LaBr}$ axis gated by different windows on the former. The choice of these windows was guided by the possible primary γ-ray transitions for each $E_{\rm LaBr}$ (Table III). By a proper choice of these windows, it is possible to suppress the contribution from some primary transitions. For example, at $E_p \sim 8$ MeV, the choice of the $E_{\rm BGO}$ window above 10.6 MeV suppresses the contributions from γ_4 and γ_5 transitions. Table IV shows some examples of

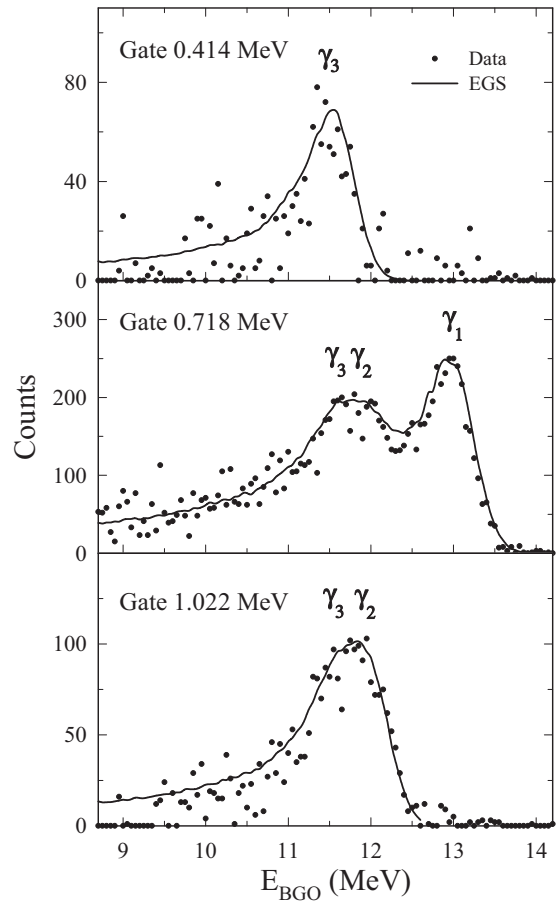

FIG. 6. BGO spectra in coincidence with the various LaBr γ rays for the 1.1 mg/cm^2 Be target at $E_p = 7.98$ MeV. The EGS simulations are also shown. Peak positions of the γ rays originating from the transitions to various excited states (γ_1 to γ_3) are indicated.

the $E_{\rm BGO}$ windows chosen for different $E_{\rm LaBr}$. Figure 7 shows an example of the projected $E_{\rm LaBr}$ spectra for different $E_{\rm BGO}$ windows.

The coincident yield for each $E_{\rm LaBr}$ was extracted for the relevant window after subtracting the pedestal contribution around the peak. The yield for a certain $E_{\rm LaBr}$ is related to the capture cross-sections mainly via the BGO-array efficiency for the chosen $E_{\rm BGO}$ window, the peak efficiency of the LaBr

TABLE IV. Examples of the $E_{\rm BGO}$ windows chosen to extract the yields in coincidence with different low-energy γ rays detected in the LaBr. W_j denotes the window used for the γ ray with the index j.

$\sim E_p$ (MeV)	W_1 W_4 W_5 (MeV)	W_2 (MeV)	W_3 (MeV)	W_6 (MeV)	W_7 (MeV)
8.0	10.6–12.2	10.7–13.8	10.6–12.8	8.7–10.7	8.0–9.2
10.0	12.4–14.2	12.4–15.6	12.4–14.7	10.9–12.8	9.2–11.1
12.0	14.1–15.9	14.1–17.4	14.1–16.5	12.6–14.4	11.1–12.8
14.0	15.8–17.6	15.8–19.3	15.8–18.3	14.3–16.3	12.5–14.8
16.0	17.6–19.5	17.6–21.1	17.6–20.1	16.0–18.0	14.1–16.4
18.0	18.6–21.3	18.6–22.8	18.6–21.8	17.4–19.8	15.6–18.2
20.0	20.6–23.1	20.6–24.8	20.6–23.7	18.6–22.0	16.8–20.9

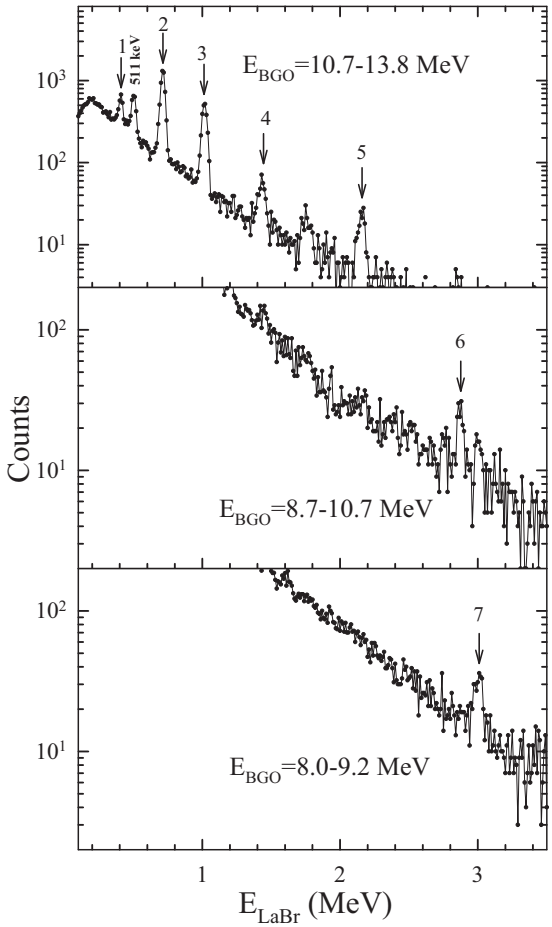

FIG. 7. LaBr spectra gated with different E_{BGO} windows for the 1.1 mg/cm^2 Be target at $E_p = 7.98$ MeV. Arrows indicate the γ rays arising from the transitions in ^{10}B. The index numbers are explained in Table III.

detectors and the branching ratios for the subsequent γ-ray transitions. In general, the yield for the jth LaBr γ-ray is given by

$$Y_j = C \sum_{s=1}^{2} \epsilon_p^j(s) \sum_{i=1}^{5} \sigma_i \left(\frac{\Gamma_\gamma}{\Gamma}\right)_i \epsilon_{\mathrm{BGO}}(i,j) \times \sum_{k=1}^{N_{\mathrm{seq}}(i,j)} P(i,j,k) \prod_{l=1}^{n_a(i,j,k)} \left[1 - \epsilon_t^l(s)\right]. \quad (2)$$

Here $\epsilon_p^j(s)$ and $\epsilon_t^j(s)$ are the peak and total efficiencies, respectively, of the sth LaBr for the jth γ ray, $\epsilon_{\mathrm{BGO}}(i,j)$ is the BGO efficiency for the primary γ ray arising from the transition to the state S_i for the E_{BGO} window chosen in coincidence with the jth γ ray, $(\Gamma_\gamma/\Gamma)_i$ is the partial γ decay width of the state S_i, and σ_i is the radiative capture cross section to be extracted. The jth γ ray can arise from the decay of the state S_i in a number of decay sequences. $N_{\mathrm{seq}}(i,j)$ denotes the number of sequences and $P(i,j,k)$ is the probability for the kth sequence—both of these were obtained from the experimentally measured branching ratios for the various interstate decays in ^{10}B [21]. There is a finite probability of one or more accompanying low-energy γ rays in a sequence simultaneously entering the LaBr detector and reducing the peak yield for a particular γ ray. The final product over the accompanying $n_a(i,j,k)$ γ rays in the kth sequence gives the probability that none of these enter the LaBr simultaneously with the jth γ ray. The constant C in Eq. (2) is given by $C = 0.42 Q_{nC} t_{mg}$ for the ^{9}Be target where Q_{nC} is the incident charge in nC, t_{mg} is the target thickness in mg/cm^2, and the extracted σ_i is in μb.

Although Eq. (2) suggests that the yield in coincidence with each E_{LaBr} γ ray is related to many σ_i values, the choice of the E_{BGO} windows, exemplified in Table IV, leads to some simplifications, as mentioned above. For example, the yields in coincidence with E_{LaBr} γ rays numbered 1, 4, and 5 are related mainly to the γ_3 transition and, hence, to σ_3. The yield in coincidence with the γ ray numbered 3 is decided mainly by σ_2 and σ_3 and, knowing σ_3, σ_2 can be obtained. After extracting σ_2 and σ_3, σ_1 is obtained from the yield in coincidence with the γ ray numbered 2 which is related to all the three cross sections. Finally σ_4 and σ_5 can be obtained from the yields in coincidence with the γ rays numbered 6 and 7.

The extracted cross sections, following the above procedures, were corrected for the effects of angular distribution of the primary γ rays and the angular correlation between the primary and the secondary γ rays. These effects, mainly decided by the former in most of the cases, are generally small because of the wide angular coverage of the detectors. The correction factors were estimated in the following approximate manner. The angular distribution of the primary γ rays was described in the usual way as

$$W(\theta) = 1 + \sum_n a_n P_n(\cos\theta), \quad (3)$$

P_n being the Legendre polynomial of order n. The angular-distribution coefficients a_n (n = 1–4) were calculated using the direct-semidirect (DSD) capture model discussed later. The DSD model calculations also provide the populations of the various magnetic substates M_f of the final state, with angular momentum J_f, for different angles of the primary γ rays. The angular-distribution coefficients of the secondary γ rays were calculated using these M_f populations. A Monte Carlo simulation was used to compute the coincidence counts in the detectors, including the above-mentioned angular-distribution coefficients of the primary and secondary γ rays. These were compared with those computed assuming an isotropic distribution for both the γ rays. The correction factors so obtained ranged from ~1 to 12% depending on the proton energy and the final state.

IV. RESULTS AND DISCUSSION

The experimentally extracted cross sections at different proton energies are shown in Figs. 8 and 9. The error bars mainly arise from the statistical errors and the uncertainties in the BGO and LaBr efficiencies. A few general comments can be made from these figures. The energy dependencies of the capture cross section for the first two excited states, having different isospin quantum numbers, are reasonably similar. Thus there is no apparent manifestation of an isospin

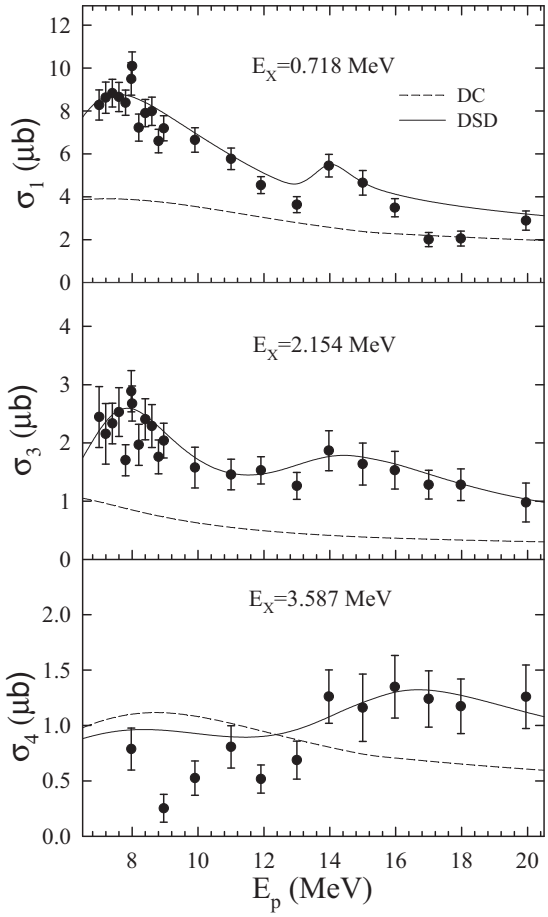

FIG. 8. Extracted capture cross sections to the $T = 0$ final states with different excitation energies E_X in ^{10}B at different proton energies. The dashed and the solid lines show the results of the calculation for the direct capture (DC) and the direct-semidirect (DSD) capture using the parameters shown in Table V.

effect in the GDR excitation built on these excited states. The maximum cross-section is seen at $E_p \sim 8$ MeV corresponding to $E_\gamma \sim 13$–14 MeV, which is much smaller than the GDR energy expected for such a light nucleus. For the other three states, the energy dependence is flatter over the measured E_p range.

In order to make a comparison of the experimental results with the earlier-measured photoneutron cross-section for the ground state of ^{10}B [22], the measured (p,γ) cross sections were converted to (γ, p_0) cross sections (leading to the ground state of ^{9}Be) using the relation

$$\sigma(\gamma, p_0) = \left(\frac{2j_t + 1}{2J_f + 1}\right)\frac{2\mu_p c^2 E_p^{\rm cm}}{E_\gamma^2}\sigma(p,\gamma), \qquad (4)$$

where J_f is the angular momentum of the final state after the radiative capture, μ_p is the reduced mass of the proton, and $E_p^{\rm cm}$ is its center-of-mass (cm) energy. These cross sections as a function of γ-ray energy are shown in Figs. 10 and 11 along with the photoneutron cross sections. The photoproton cross sections (leading to the ground state of ^{9}Be) for the excited states of ^{10}B are markedly different from the photoneutron

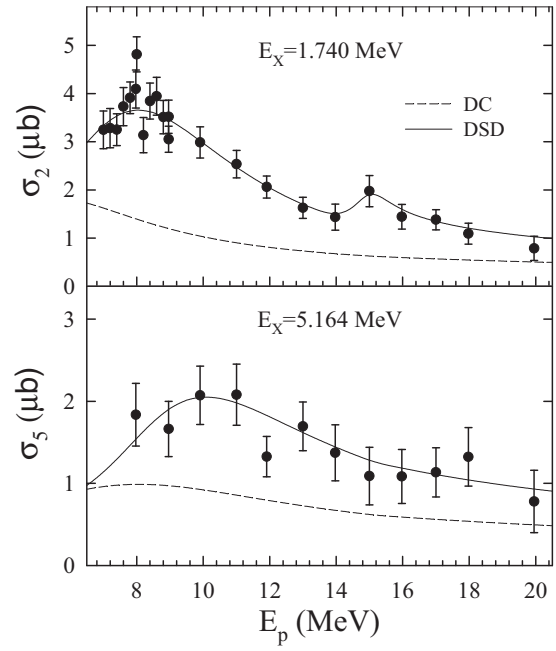

FIG. 9. Same as in Fig. 8 but for the $T = 1$ final states in ^{10}B.

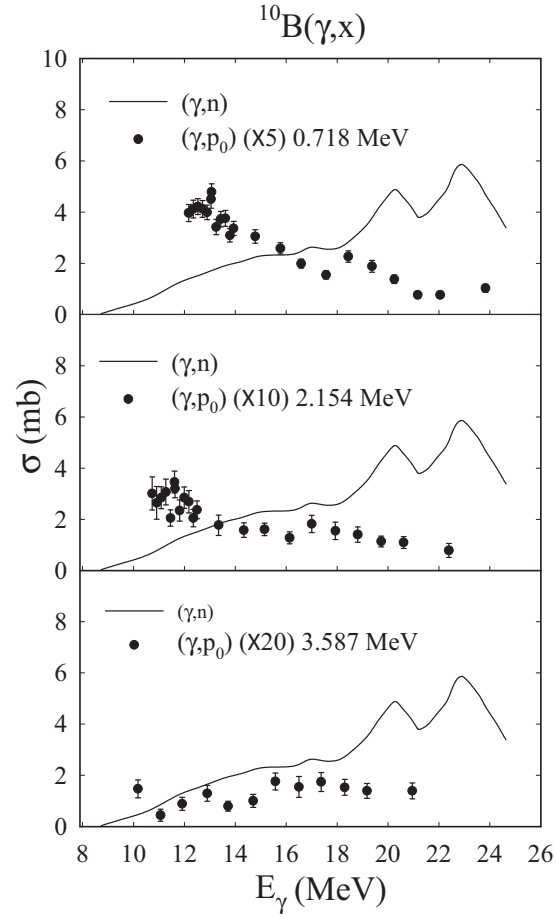

FIG. 10. Derived photoproton cross sections for the $T = 0$ states in ^{10}B at different γ-ray energies. The solid line is a smooth curve drawn through the earlier measured photoneutron cross sections for ^{10}B.

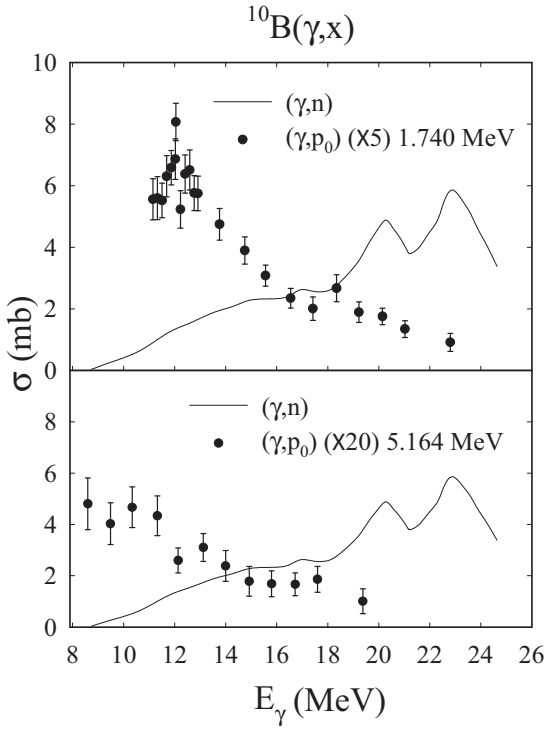

FIG. 11. Same as in Fig. 10 but for the $T = 1$ states in ^{10}B.

cross sections for the ground state, both in magnitude and in shape. If the excited nucleus decays statistically after the photoabsorption, the total photoproton cross section should be more than the (γ, p_0) cross sections by a factor which increases with γ-ray energy. The reason for this is the opening of more decay channels at a higher excitation energy and a consequent lower decay branch to the ground state. However, if the decay is not statistical, as expected for light nuclei, the total photoproton cross section would be larger but should not show a drastic dependence on the excitation energy. In other words, one can infer that the profile of the total photoabsorption cross section is very different for the excited states of ^{10}B compared to that for the ground state. This, however, is observed for both $T = 0$ and $T = 1$ excited states. (The present data, of course, do not address the photoproton cross section for the ground state of ^{10}B).

We now try to describe the measured cross sections using a relatively simple model, viz., the DSD capture model [23,24]. In this model, there are two processes (and hence two amplitudes) contributing to the cross section, one being the direct capture of the incoming proton to the final state and the other via the excitation of the intermediate giant resonance configurations. The final state wave function, therefore, should have a reasonably good overlap with the (target + proton) configuration. In other words, the proton spectroscopic factor should have a reasonably large value.

The capture cross section within the DSD model was calculated following the formalism described in detail in our earlier papers [9,25]. In the direct capture part, only the electric multipoles with multipolarity $L \leqslant 4$ were included. In the semidirect part, only the GDR excitation was considered. The inclusion of the isoscalar and isovector giant quadrupole excitations, however, changes the result by at best 5%. In the present work, we included the two-component GDR excitation by adding the amplitudes corresponding to each component to the direct part. The important inputs in these calculations are the OMP parameters for calculating the incoming proton wave function, the final state spectroscopic factors (S_f), the GDR energies (E_{D1} and E_{D2}), GDR widths (Γ_{D1} and Γ_{D2}), fractions of the classical sum-rule limit (SRL) exhausted (S_{D1} and S_{D2}) in the two components, and the depth of the isovector potential (V_1) responsible for the excitation of the GDR in the intermediate state.

The OMP parameters were taken from Ref. [26]. The radius and diffuseness parameters for the bound state potential of the final states were the same as those of the real part of the OMP and the depth was adjusted to get the appropriate binding energies. The value of V_1 was fixed at 108 MeV, consistent with the OMP parameters. The S_f values were based on the experimental and theoretical results [27,28]. The GDR parameters were varied to get the fit to the experimental cross sections. The results of the DSD model calculations are shown in Figs. 8 and 9 by the dashed and the solid curves for the direct capture and the direct-semidirect capture, respectively. The best-fit parameters describing the experimental data are given in Table V. The error bars presented in the table were calculated by varying one parameter at a time and keeping all other parameters at the best-fit values.

The overall agreement of the data with the DSD model calculations is reasonably good as shown by the solid lines in Figs. 8 and 9. A small excess around $E_p = 8$ MeV, for the decay to the 0.718 and 1.740 MeV states, could be due to the presence of some structures around the corresponding excitation energies. If these excess yields also have the $E1$ multipolarity, the states corresponding to these structures should be different because their isospin values should be $T = 1$ and 0, respectively. The present data, however, are not capable of providing any further insight on this aspect.

The comparison of the extracted average GDR energy (∼12 MeV) for the $T = 1$ state at 1.74 MeV with the ground-state GDR energy (∼22 MeV; see Figs. 10 and 11) indicates a large decrease for the former. It should be noted that the fraction of the SRL exhausted in this case is approximately that expected for the split strength of the $T_{\rm GDR} = 0$ component built on the $T = 1$ state [7]. For the $T = 0$ state at 0.718 MeV, the GDR energy and strength are similar to those for the 1.74 MeV state. However, in this case, there is no isospin splitting of the strength. The exhaustion of ∼30% of the SRL in this case could imply that the $E1$ strength is distributed over still higher excitation energies, making the average GDR energy higher. From the present data, however, we cannot make a definite comment on the average GDR energy for this state. Thus, although the first comparison above could imply a large isospin effect in the GDR excitation, the second observation weakens the conclusion because one cannot discard a decrease seen for the excited $T = 0$ state also. The GDR parameters for the other excited states do not show any systematic variation with excitation energy. For the third excited state, the average GDR energy is higher because the higher-energy component has a larger strength and ∼60% of SRL is exhausted in this case.

TABLE V. Important parameters used in the DSD model calculations. E_X is the final state excitation energy and nlj is the single-particle configuration. Other parameters are explained in the text. The last row shows the references for the S_f values used. All energies are in MeV.

E_X	0.718	1.740	2.154	3.587	5.164
nlj	$1p_{3/2}$	$1p_{3/2}$	$1p_{3/2}$		$1p_{3/2}$
	$1p_{1/2}$			$1p_{1/2}$	$1p_{1/2}$
S_f	0.35	1.38	0.30		0.05
	0.65			0.23	0.23
E_{D1}	$11.3^{+0.6}_{-1.1}$	$11.3^{+0.5}_{-0.3}$	$11.0^{+0.4}_{-0.8}$		$8.8^{+1.0}_{-3.0}$
Γ_{D1}	4.1 ± 0.4	6.3 ± 0.5	3.8 ± 0.6		6.0 ± 1.5
S_{D1}	0.26 ± 0.03	0.34 ± 0.04	0.24 ± 0.03		0.29 ± 0.06
E_{D2}	18.2 ± 0.3	18.2 ± 0.4	16.9 ± 0.9	16.5 ± 0.7	
Γ_{D2}	1.4 ± 0.4	1.3 ± 0.5	6.0 ± 1.5	6.8 ± 1.6	
S_{D2}	0.03 ± 0.01	0.03 ± 0.02	0.36 ± 0.09	0.26 ± 0.08	
Ref. (S_f)	[27][a]	[27]	[27]	[27]	[28]

[a]Relative S_f for $1p_{3/2}$ and $1p_{1/2}$ states are taken from [28].

The parameter sets for the highest two excited states are also very different. The $E1$ strength functions built on the excited states, therefore, appear to be dependent on the structure of the excited states. This trend is generally expected for very light nuclei. A microscopic calculation of the multipole strength functions is required to understand the experimental results, particularly, the big difference with the strength function built on the ground state. Measurements at higher proton energies also would provide more insight into these issues.

V. SUMMARY

In summary, the cross sections of the radiative proton capture reaction ^{9}Be(p,γ), populating five low-lying excited states of ^{10}B with different isospin, have been measured over the proton energy range of 7–20 MeV. For this purpose, the method of coincidence between the primary γ rays, emitted after the proton capture to the low-lying states, and the secondary γ rays, emitted from the subsequent decay of these states, was used. The motivation behind these measurements was to address the GDR built on the isospin $T = 0$ and $T = 1$ states in the self-conjugate nucleus ^{10}B and, hence, to address the isospin effects in the GDR excitation. The measured cross sections for the first two excited states, having $T = 0$ and 1, respectively, show a reasonably similar proton-energy dependence. The DSD capture model calculations were performed for the cross sections. The GDR parameters describing the data for the first two excited states are reasonably similar but are different for the other three states. Whereas the present work establishes that the $E1$-strength distributions built on the five excited states are dependent on the structure of the states, it does not manifest any conclusive isospin effect in the GDR excitation. The derived inverse photoproton cross sections for all five excited states are very different from the earlier-measured photoneutron cross sections for the ground state.

ACKNOWLEDGMENTS

The present work was done under Project No. SR/S2/HEP-0037/2012 assigned to one of the authors (D.R.C.) by the Science and Engineering Research Board, Department of Science and Technology, Government of India. The authors thank S. P. Behera, A. Mitra, A. Bhattacharya, and Sukanya De for their help during the experiment, the accelerator staff for the smooth operation of the machine, and R.G. Thomas for performing the GEANT calculations.

[1] K. A. Snover, Annu. Rev. Nucl. Part. Sci. **36**, 545 (1986) and references therein.
[2] K. A. Snover, *Neutron Capture Gamma Ray Spectroscopy* (Plenum, New York, 1979), p. 319, and references therein.
[3] J. J. Gaardhøje, Annu. Rev. Nucl. Part. Sci. **42**, 483 (1992).
[4] M. N. Harakeh and A. van der Woude, *Giant Resonances: Fundamental High-Frequency modes of Nuclear Excitation* (Oxford Science, Oxford, 2001).
[5] D. R. Chakrabarty, N. D. Dang, and V. M. Datar, Eur. Phys. J. A **52**, 143 (2016).
[6] M. B. Johnson and C. L. Morris, Annu. Rev. Nucl. Part. Sci. **43**, 165 (1993) and references therein.
[7] F. Reiss, W. J. O'Connell, and P. Paul, Nucl. Phys. A **175**, 462 (1971).
[8] P. Paul, H. S. Kuan, and E. K. Warburton, Nucl. Phys. A **254**, 1 (1975).
[9] D. R. Chakrabarty, V. M. Datar, Suresh Kumar, E. T. Mirgule, A. Mitra, V. Nanal, and H. H. Oza, Phys. Rev. C **69**, 021602(R) (2004).
[10] D. R. Chakrabarty, V. M. Datar, Suresh Kumar, E. T. Mirgule, A. Mitra, V. Nanal, and P. C. Rout, Phys. Rev. C **77**, 051302(R) (2008).
[11] E. Van Camp, D. Ryckbosch, R. Van de Vyver, E. Kerkhove, P. Van Otten, and P. Berkvens, Phys. Rev. C **30**, 1182 (1984) and references therein.

[12] V. V. Varlamov, N. N. Pescov, and M. E. Stepanov, Phys. At. Nucl. **72**, 214 (2009) and references therein.
[13] D. R. Tilley, J. H. Kelley, J. L. Godwin, D. J. Millener, J. E. Purcell, C. G. Sheu, and H. R. Weller, Nucl. Phys. A **745**, 155 (2004).
[14] F. Ajzenberg-Selove, Nucl. Phys. A **490**, 1 (1988) and references therein.
[15] W. R. Nelson, H. Hirayama, and D. W. O. Rogers, Stanford University Report No. SLAC 265, 1985 (unpublished).
[16] S. Agostinelli *et al.* (GEANT4 Collaboration), Nucl. Instrum. Methods A **506**, 250 (2003).
[17] R. G. Allas, S. S. Hanna, L. Meyer-Schutzmeister, and R. E. Segel, Nucl. Phys. **58**, 122 (1964).
[18] P. P. singh, R. E. Segel, L. Meyer-Schutzmeister, S. S. Hanna, and R. G. Allas, Nucl. Phys. **65**, 577 (1965).
[19] F. C. Erne, Nucl. Phys. **84**, 241 (1966).
[20] F. G. Perey, Phys. Rev. **131**, 745 (1963).
[21] E. A. McCutchan, C. J. Lister, M. Elvers, D. Savran, J. P. Greene, T. Ahmed, T. Ahn, N. Cooper, A. Heinz, R.O. Hughes, G. Ilie, B. Pauerstein, D. Radeck, N. Shenkov, and V. Werner, Phys. Rev. C **86**, 057306 (2012).
[22] M. H. Ahsan, S. A. Siddiqui, and H. H. Thies, Nucl. Phys. A **469**, 381 (1987).
[23] G. E. Brown, Nucl. Phys. **57**, 339 (1964).
[24] C. F. Clement, A. M. lane, and J. R. Rook, Nucl. Phys. **66**, 273 (1965); **66**, 293 (1965).
[25] D. R. Chakrabarty, V. M. Datar, Y. K. Agarwal, C. V. K. Baba, M. S. Samant, I. Mazumdar, A. K. Sinha, and P. Sugathan, Phys. Rev. C **60**, 024606 (1999) and references therein.
[26] B. A. Watson, P. P. Singh, and R. E. Segel, Phys. Rev. **182**, 977 (1969).
[27] S. M. Lukyanov *et al.*, J. Phys. G **41**, 035102 (2014).
[28] S. Cohen and D. Kurath, Nucl. Phys. A **101**, 1 (1967).